Supporting Information

Enhanced Visible Photovoltaic Response of TiO_2 Thin Film with an All-Inorganic Donor-Acceptor Type Polyoxometalate

Jian-Sheng Li,[†,§] *Xiao-Jing Sang,*[†,§] *Wei-Lin Chen,*[*,†] *Lan-Cui Zhang,*[‡] *Zai-Ming Zhu,*[‡] *Teng-Ying Ma,*[†] *Zhong-Min Su*[†] *and En-Bo Wang*[*,†]

[†]Key Laboratory of Polyoxometalate Science of Ministry of Education, Department of Chemistry, Northeast Normal University, Changchun, Jilin 130024, (China).

[§] School of Chemistry and Chemical Engineering, Liaoning Normal University, Dalian 116029.

E-mail: wangeb889@nenu.edu.cn; chenwl@nenu.edu.cn

Section 1 Energy Level Regulation for thirteen POMs

1.1 FTIR spectra

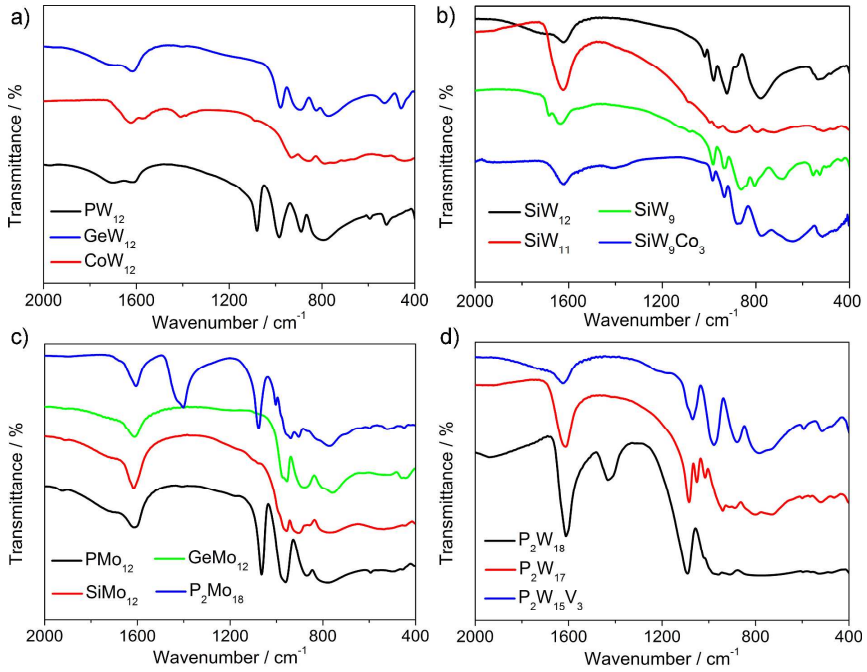

Figure S1 FTIR spectra of fourteen kinds of POMs: a) FTIR spectra of PW_{12} (dark line), GeW_{12} (blue line), CoW_{12} (red line); b) FTIR spectra of SiW_{12} (dark line), SiW_{11} (red line); SiW_9Co_3 (blue line); SiW_9 (green line); c) FTIR spectra of PMo_{12} (dark line), $SiMo_{12}$ (red line), $GeMo_{12}$ (green line), P_2Mo_{18} (blue line); d) FTIR spectra of P_2W_{18} (dark line), P_2W_{17} (red line), $P_2W_{15}V_3$ (blue line)

Figure S1 showed the FTIR spectra of POMs. It can be seen from Figure S1a, for PW_{12}, there were four characteristic peaks in the range of 800-1100cm^{-1} at 802, 889, 984 and 1082 cm^{-1}, which were attributed to W–O_c–W asymmetric stretching vibrations, W–O_b–W bending vibrations, W–O_t bending vibrations and P–O_a asymmetric stretching vibrations, (O_d, terminal O atoms; O_b, O_c, bridging O atoms), respectively. Figure S1b showed the FTIR spectra of SiW_{12} and SiW_{11}. The four characteristic peaks of SiW_{12} at 781, 881, 923 and 981 cm^{-1} were assigned to W–O_c–W asymmetric stretching vibrations, W–O_b–W bending vibrations, Si–O_a asymmetric stretching vibrations and W–O_t bending vibrations, respectively. Meanwhile, the four characteristic peaks splitted into more peaks from SiW_{12} to SiW_{11}, illustrating that the structure symmetry of POMs were lowered. As can be seen from Figure S1b, the characteristic vibrations of ν(W–O_t), ν(W–O_b–W), ν(Si–O_a) and ν(W–O_c–W) of SiW_9Co_3 appear at 986, 935, 877 and 774 cm^{-1},

respectively, which confirmed the structure of SiW_9Co_3. Figure S1c were the FTIR spectra of PMo_{12}, $SiMo_{12}$, $GeMo_{12}$ and P_2Mo_{18}, in which the four characteristic peaks confirmed their structures. In Figure S1d, the more characteristic peaks for P_2W_{17} than P_2W_{18} were attributed to its lacunary structure and the four characteristic peaks for $P_2W_{15}V_3$ were resulted from the substitution of transitional metals, which increased the symmetry of the lacunary structure.

1.2 Raman spectra

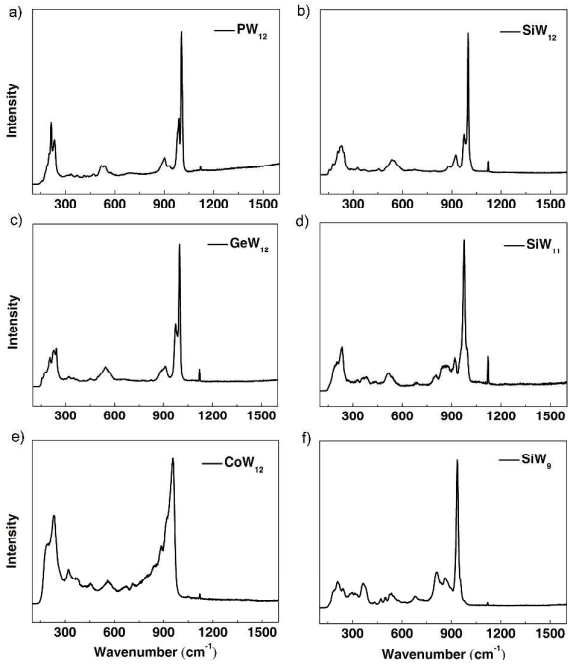

Figure S2 The normal Raman spectrum for a) PW_{12}, b) SiW_{12}, c) GeW_{12}, d) SiW_{11}, e) CoW_{12} and f) SiW_9

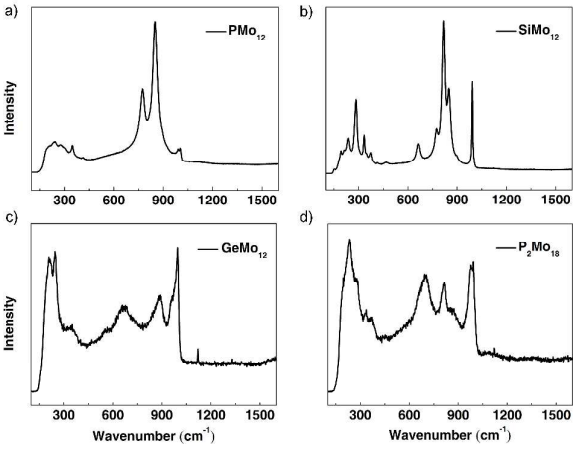

Figure S3 The normal Raman spectrum for a) PMo_{12}, b) $SiMo_{12}$, c) $GeMo_{12}$ and d) P_2Mo_{18}

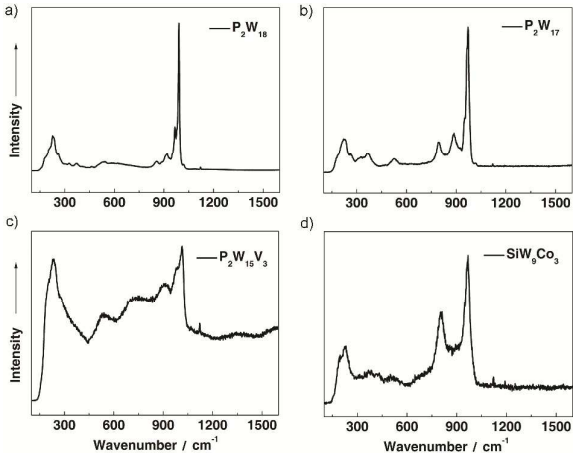

Figure S4 The normal Raman spectrum for a) P_2W_{18}; b) P_2W_{17}; c) $P_2W_{15}V_3$ and d) SiW_9Co_3

Raman spectrum (Figure S2-S4) could also provide the information about the structures of POMs by researching their vibration and rotation energy as a kind of scattering spectrum. In Figure S2b, the bands between 900 and 1000 cm^{-1} were associated with the stretching mode of W-O_t. The bands from 800 to 900 cm^{-1} corresponded to the stretching mode of W-O_b-W or W-O_c-W. The lower energy regions were due to the bending mode of W-O_b-W or W-O_c-W or Si-O. The normal Raman spectra of the Keggin anions were consistent with the reported values, which further confirmed the structures of POMs. The bands of lacunary structures experienced peak splitting because of the lower symmetry. The band positions shifted slightly due to the substitution of transitional metals.

1.3 TG Curves

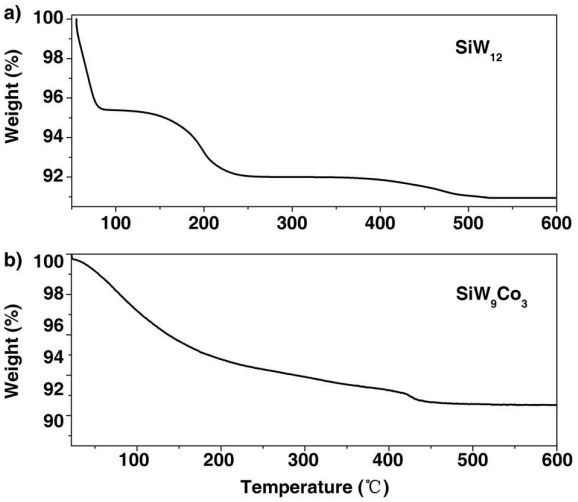

Figure S5 TG curves of a) SiW_{12} and b) SiW_9Co_3

As shown in the TG curves (Figure S5), three-step weight loss occurred for both compounds in the

temperature range from 30 ℃ to 600 ℃ under N_2 condition. The three-step weight losses were all attributed to the loss of water molecular, demonstrating that the skeleton structures of POMs remained unchanged during this temperature range, and the stable temperature lasted until around 500 and 440 ℃ for SiW_{12} and SiW_9Co_3, respectively. The results demonstrated that POMs had very good thermal stability.

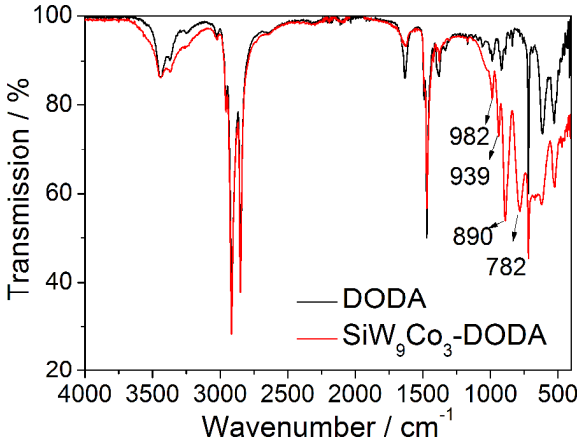

Figure S6 FTIR spectrum of DODA (dark line) and $DODA^+$ encapsulated SiW_9Co_3 composite (red line)

The FTIR spectrum of $DODA^+$ encapsulated SiW_9Co_3 was given to detect its composition. As shown in Figure S6, after embedding with $DODA^+$, the framework of SiW_9Co_3 remained intact with its characteristic vibrations of $\nu(W\text{-}O_t)$, $\nu(W\text{-}O_b\text{-}W)$, $\nu(Si\text{-}O_a)$ and $\nu(W\text{-}O_c\text{-}W)$ at 982, 939, 890, and 782 cm^{-1}, respectively. The slight shift on high wavenumber compared with SiW_9Co_3 was due to the electrostatic attraction between SiW_9Co_3 anion and $DODA^+$. Besides, the characteristic peak of $DODA^+$ at 1470 cm^{-1} demonstrated the successful embedding by $DODA^+$.

1.4 Optical Band Gap

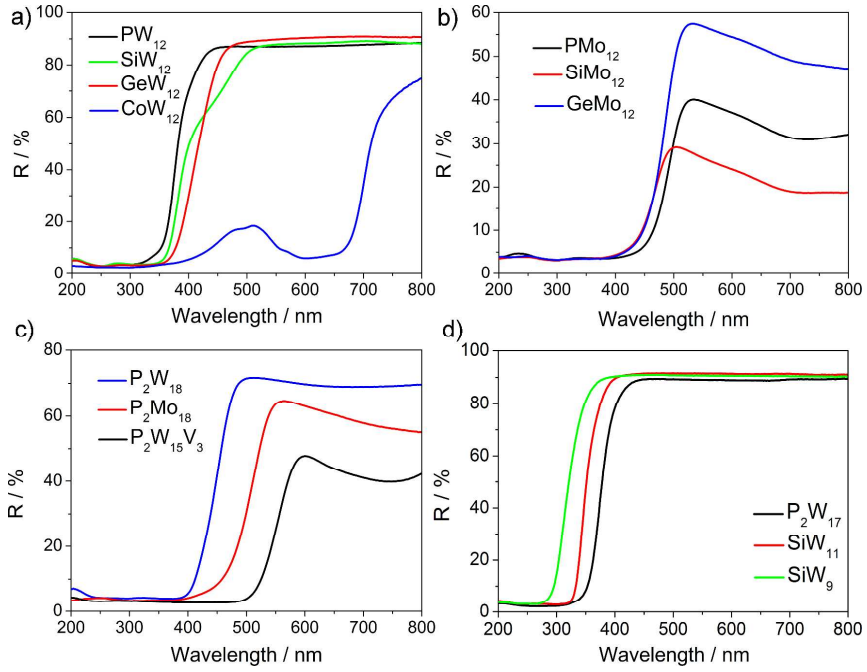

Figure S7 The diffuse reflection spectrums of POMs: a) PW_{12} (dark line), SiW_{12} (green line), GeW_{12} (red line), CoW_{12} (blue line); b) PMo_{12} (dark line), $SiMo_{12}$ (red line), $GeMo_{12}$ (blue line); c) P_2Mo_{18} (red line), P_2W_{18} (blue line), $P_2W_{15}V_3$ (dark line); d) P_2W_{17} (dark line), SiW_{11} (red line), SiW_9 (green line)

The optical band gaps of POMs could be estimated with the diffuse reflection spectrums shown in Figure S7. Firstly, a plot of Kubelka-Munk function F against energy E was drawn, in which F can be obtained by Equation S1, in which R is the reflectance of an infinitely thick layer at a given wavelength. The band gap E_g was determined as the intersection point between the energy axis and the line extrapolated from the linear portion of the absorption edge in the plot of F against energy E (Figure S8).[S1] The obtained E_g of all the samples by this way were listed in Figure 1.

$$F = (1-R)^2 / 2R \quad (Equation\ \ S1)$$

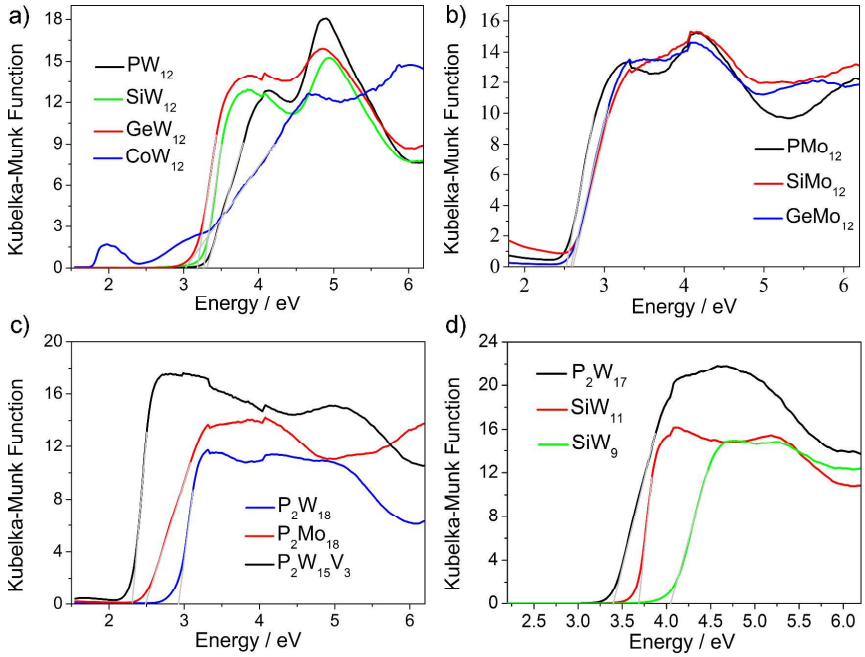

Figure S8 The plot of K-M function *F* against energy *E*: a) PW_{12} (dark line), SiW_{12} (green line), GeW_{12} (red line), CoW_{12} (blue line); b) PMo_{12} (dark line), $SiMo_{12}$ (red line), $GeMo_{12}$ (blue line); c) P_2Mo_{18} (red line), P_2W_{18} (blue line), $P_2W_{15}V_3$ (dark line); d) P_2W_{17} (dark line), SiW_{11} (red line); SiW_9 (green line)

1.5 The LUMO Level

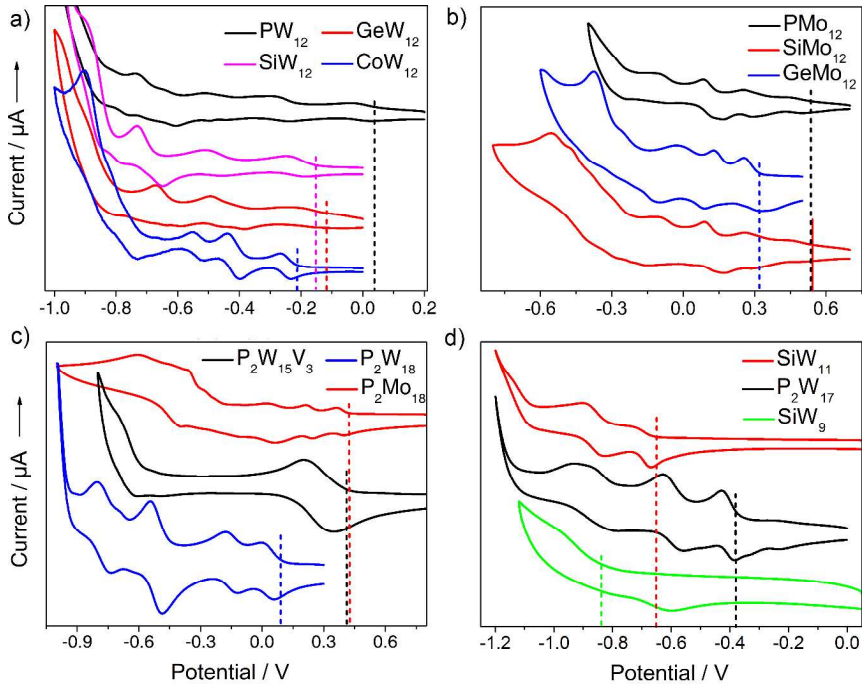

Figure S9 The cyclic voltammograms of POMs: a): PW_{12} (dark line), SiW_{12} (pink line), GeW_{12}

(red line), CoW_{12} (blue line); b) PMo_{12} (dark line), $SiMo_{12}$ (red line), $GeMo_{12}$ (blue line); c) P_2W_{18} (blue line), P_2Mo_{18} (red line), $P_2W_{15}V_3$ (dark line); d) SiW_{11} (red line), P_2W_{17} (dark line), SiW_9 (green line). The intersection point of dot line and X axis corresponded to the onset reduction potential of POMs. The conditions of the electrolyte solution during electrochemical test for various kinds of POMs were listed in Table S2.

Because the LUMOs of POMs are formally a nonbonding combination of symmetry-adapted dxy like orbits centering on the metal (W) atoms,[S2] the LUMO levels could be estimated by finding out the applied onset potential for the first reduction of POMs,[S3] and the HOMOs could be calculated according to Equation S2:

$$E\,[LUMO(vs\ Vaccum)] = E\,[HOMO(vs\ Vaccum)] + E_g \quad (Equation\ S2)$$

Meanwhile, it is known that the reduction potentials of POMs in the cyclic voltammograms are dependent on the test environment, especially influenced by the pH of the electrolyte solution. Therefore, all the electrochemical experiments were carried out in the system of H_2O solution and the same electrolyte and pH value were selected on the premise of guarantee of their stability for various series of POMs to eliminate the significant influence on the electrochemical response as far as possible. Based on this, the ground and excited energy levels of POMs could be measured and calculated (Figure 1).

Section 2 Physical and Chemical Characterization

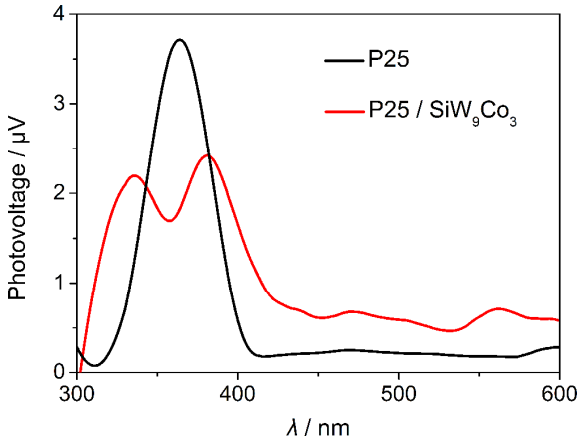

Figure S10. The SPV spectroscopy for P25 (dark line) and P25/SiW_9Co_3 composite (red line)

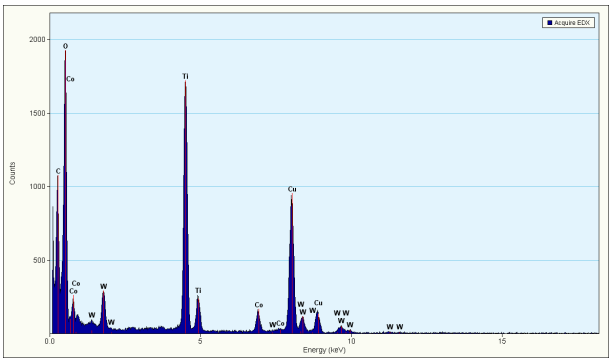

Figure S11 EDS from $DODA^{+}$ encapsulated SiW_9Co_3 adsorbed TiO_2 film

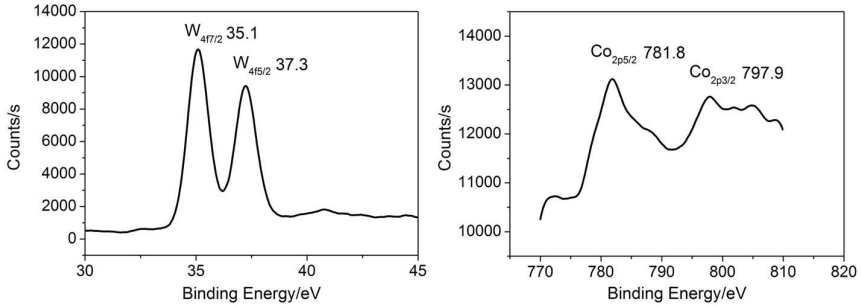

Figure S12 XPS spectrum of the isolated SiW_9Co_3 powder for W and Co energy level

The XPS spectrum of the isolated SiW_9Co_3 powder for W and Co energy level were carried out to evaluate the stability of SiW_9Co_3 that adsorbed on the titanium dioxide films. In the XPS spectrum of SiW_9Co_3 powder (Figure S12), the two peaks of W_{4f} at ca. 35.1 and 37.3 eV were ascribed to the binding energy of $W_{4f7/2}$ and $W_{4f5/2}$, which corresponded to the oxidation state of W^{VI}. The XPS spectrum for Co_{2p} showed two peaks at ca. 781.8 eV and 797.9 eV resulted from the energy region of $Co_{2p3/2}$ and $Co_{2p1/2}$, which were consistent with the oxidation state of Co^{II}. The results demonstrated that SiW_9Co_3 was stable during its incorporation in TiO_2 film.

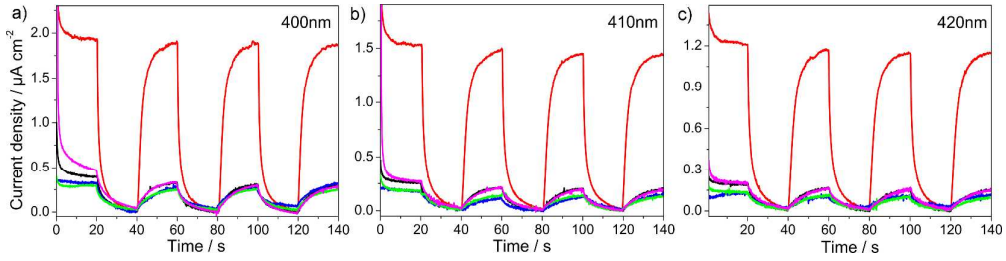

Figure S13 The photocurrent density-time curves of SiW_{12} (pink line), SiW_{11} (green line), SiW_9 (blue line), and SiW_9Co_3 (red line)-adsorbed TiO_2 electrode and bare TiO_2 electrode (dark line) under irradiation at a) 400nm, b) 410nm and c) 420 nm, respectively.

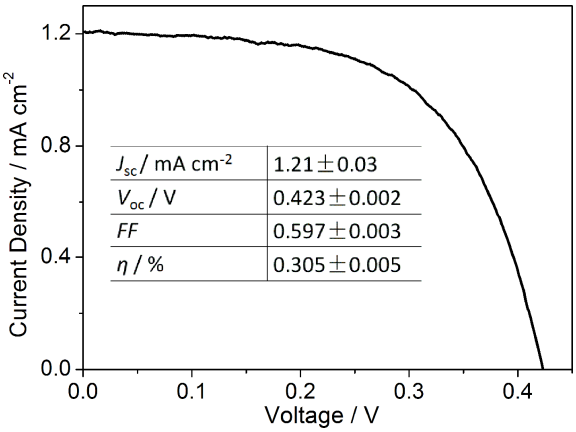

Figure S14 The current–voltage characteristic of the two-electrode system cell from the SiW_9Co_3 adsorbed TiO_2 film

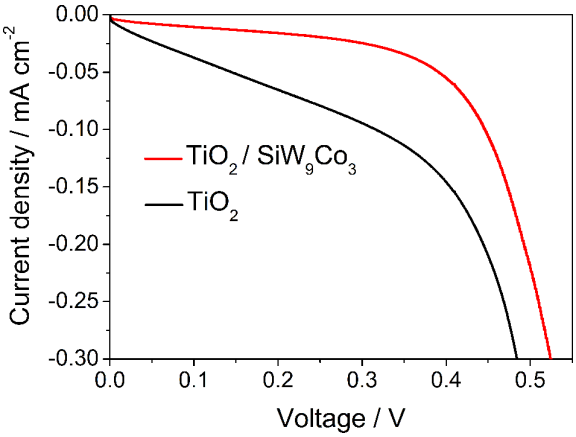

Figure S15 The dark current density characteristic of SiW_9Co_3-adsorbed (red line) and bare TiO_2-based (dark line) solar cell

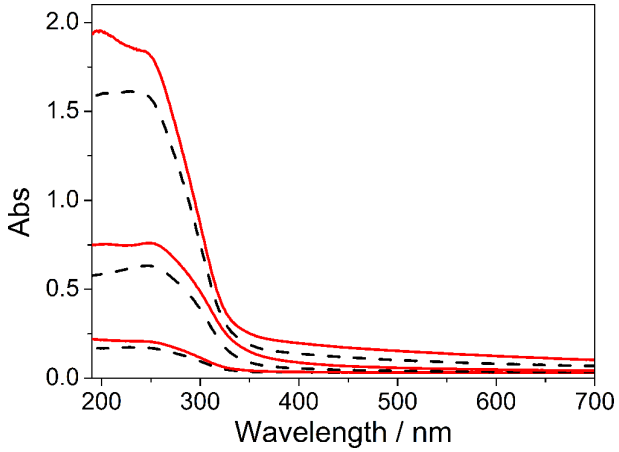

Figure S16 UV-vis absorption spectra of multilayer films {TiO_2/SiW_9Co_3}n on quartz substrates with n = 1-3 (from lower to upper curves)

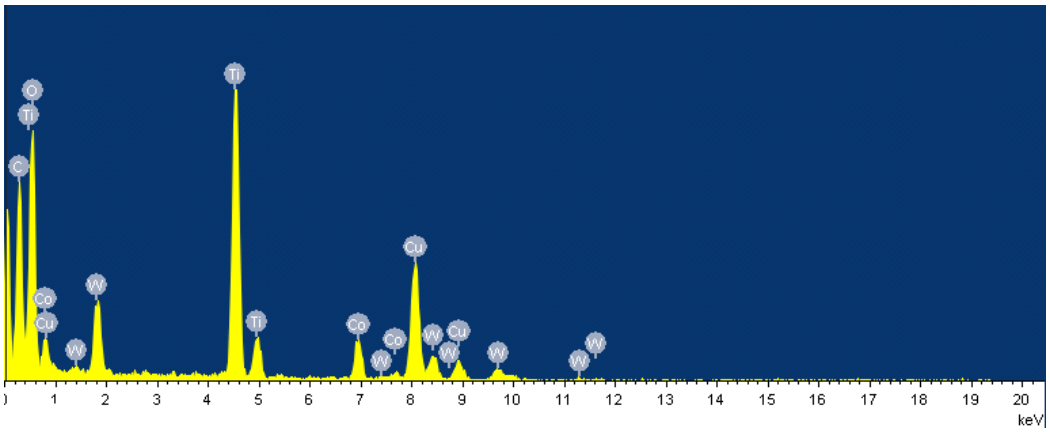

Figure S17 Energy-dispersive spectrometry (EDS) of $\{TiO_2/SiW_9Co_3\}_3$ nanocomposite film

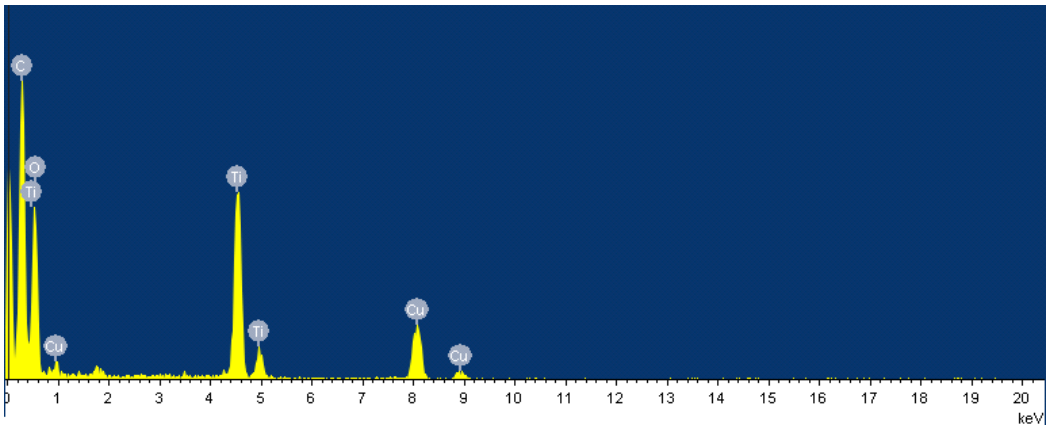

Figure S18 EDS of TiO_2 nanocrystalline film

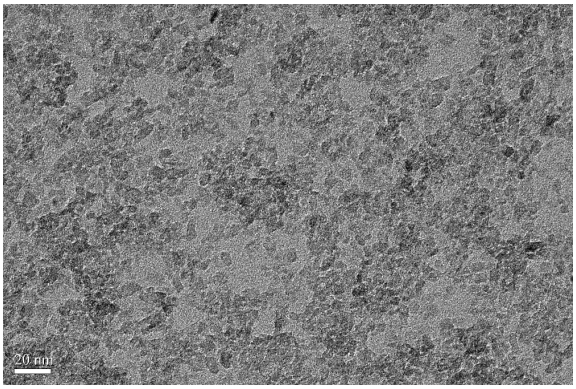

Figure S19 TEM image of TiO_2 nanocrystalline film from the layer-by-layer process

Section 3 Tables

Table S1. The electrochemical measurement conditions of various POMs

Electrolyte	Concentration (M)	pH	Type of POMs [a]
Na_2SO_4/H_2SO_4	0.1	1.5	PW_{12}; GeW_{12}; SiW_{12}; CoW_{12}; PMo_{12}; $SiMo_{12}$; $GeMo_{12}$
Na_2SO_4/H_2SO_4	0.1	2.0	P_2W_{18}; P_2Mo_{18}; $P_2W_{15}V_3$
NaAc/HAc	0.1	4.5	P_2W_{17}; SiW_{11};
LiAc/HAc	0.5	6.0	SiW_9Co_3
NaAc/HAc	0.1	6.5	SiW_9

[a] The concentrations of all the POMs are 0.5 mM.

Table S2. Photovoltaic parameters of the two-electrode cells constructed from SiW_9Co_3 adsorbed TiO_2 film

	J_{sc} / mA cm^{-2}	V_{oc} / V	*FF*	η / %	Average / %
SiW_9Co_3 / TiO_2	1.24	0.421	0.594	0.310	0.305±0.005
	1.21	0.423	0.597	0.305	
	1.20	0.425	0.595	0.303	

Table S3. Photovoltaic parameters of DSSCs with and without $\{TiO_2/SiW_9Co_3\}_3$ nanocomposite film

	J_{sc} / mA cm^{-2}	V_{oc} / V	*FF*	η / %	Average / %
Cell 1	18.3	0.757	0.620	8.59	8.53±0.06
	18.1	0.758	0.622	8.53	
	17.9	0.762	0.623	8.50	
Cell 2	15.6	0.706	0.618	6.81	6.79±0.05
	15.6	0.705	0.617	6.79	
	15.4	0.708	0.618	6.74	

References

[S1] Zhai, Q. G.; Wu, A. Y.; Chen, S. M.; Zhao, Z. G.; Lu, C. Z. Construction of Ag/1,2,4-Triazole/Polyoxometalates Hybrid Family Varying from Diverse Supramolecular

Assemblies to 3-D Rod-Packing Framework. *Inorg. Chem.* **2007**, *46* (12), 5046-5058.

[S2] Lopez, X.; Fernandez, J. A.; Poblet, J. M. Redox Properties of Polyoxometalates: New Insights on the Anion Charge Effect. *Dalton. Trans.* **2006,** (9), 1162-1167.

[S3] Li, Y. C.; Zhong, H. Z.; Li, R.; Zhou, Y.; Yang, C. H.; Li, Y. C. High-Yield Fabrication and Electrochemical Characterization of Tetrapodal CdSe, CdTe, and $CdSe_xTe_{1-x}$ Nanocrystals. *Adv. Funct. Mater.* **2006**, *16* (13), 1705-1716.